J. Fluid Mech. (2008), *vol.* 613, *pp.* 385–394.
doi:10.1017/S0022112008003571 Printed in the United Kingdom

The effect of the slope of irregularly distributed roughness elements on turbulent wall-bounded flows

E. NAPOLI[1], V. ARMENIO[2]† AND M. DE MARCHIS[1]

[1]Dipartimento di Idraulica e Applicazioni Ambientali, Universitá di Palermo, Palermo, 90128, Italy

[2]Dipartimento di Ingegneria Civile e Ambientale, Universitá di Trieste, 34127 Trieste, Italy

(Received 14 March 2008 and in revised form 28 July 2008)

Wall roughness produces a downward shift of the mean streamwise velocity profile in the log region, known as the *roughness function*. The dependence of the roughness function on the height and arrangement of roughness elements has been confirmed in several studies where regular rough walls were analysed; less attention has been paid to non-regular rough walls. Here, a numerical analysis of turbulent flows over irregularly shaped rough walls is performed, clearly identifying the importance of a parameter, called the *effective slope* (ES) of the wall corrugations, in characterizing the geometry of non-smooth irregular walls. The effective slope proves to be one of the fundamental geometric parameters for scaling the roughness function. Specifically, for a moderate range of roughness heights, both in the transitionally and in the fully rough regime, ES appears to scale the roughness function for a wide range of irregular rough geometric configurations. The effective slope determines the relative importance of friction drag and pressure drag. For $ES \sim 0.15$ we find that the friction contribution to the total wall stress is nearly in balance with the pressure-drag contribution. This value separates the region where the roughness function $\Delta U^+ = f(ES)$ is linear from that where a smooth nonlinear behaviour is observed. In the cases investigated, value $ES \sim 0.15$ also separates the transitionally rough regime from the fully rough regime.

1. Introduction

Turbulent flows of engineering, geophysical and environmental interest are frequently bounded by solid rough walls. Although in nature the wall roughness geometry is characterized by an irregular shape, with randomly distributed elements having different height, most experimental and numerical analyses of rough-wall turbulent flows have been focused on ordered arrangements of roughness elements. This choice has been mainly driven by the need to understand the modifications of the turbulent flow by the series of indentations in the walls. The use of irregular roughness also makes it difficult to identify universal geometrical parameters to characterize the shape of the walls. An additional problem is the difficulty in obtaining detailed measurements of hydrodynamic quantities very close to a rough wall or performing numerical simulations in the presence of complex boundary shapes.

One of the main effects of a rough wall on the turbulent flow is known to consist of the downward shift of the streamwise mean velocity profile in the log region, compared

† Author to whom correspondence should be addressed: armenio@dic.units.it

to a smooth wall, corresponding to an increase of the drag coefficient $C_D = \tau_s / 0.5\rho U_0^2$ with τ_s the total wall stress, ρ the fluid density and U_0 the bulk velocity of the flow. This shift is quantified with the *roughness function* ΔU^+ (hereafter the superscript $^+$ denotes variables made non-dimensional with inner variables $u^* = \sqrt{\tau_s/\rho}$ and ν/u^*, where ν is the kinematic viscosity). For surfaces roughened with individual elements of identical shape and dimensions, ΔU^+ was found to depend on the height k^+ of the elements in wall units and on other geometric features, such as their density (the number of elements per unit area) and shape. The importance of the density of roughness elements was clearly identified by Colebrook & White (1937), who found that the number of roughness elements protruding from the viscous boundary layer affects the overlying flow. Shockling, Allen & Smits (2006) characterized sand grain roughness using the distance between the higher elements, thus partially accounting for their density. In order to quantify the density of roughness elements, Schlichting (1936) defined the solidity $\lambda = F_r/F$ as the ratio between the total projected frontal roughness area (F_r) and the wall-parallel projected area (F). For regularly roughened surfaces, the ratio k_s/k between the equivalent sand roughness k_s and the height k of the elements was found to correlate very well with the solidity. To account for the shape of the roughness elements, which is not taken in consideration in the solidity, for regular roughness with identical elements, Sigal & Danberg (1990) defined the roughness parameter:

$$\Lambda_s = \frac{F}{F_r}\left(\frac{A_f}{A_s}\right)^{-1.6} \tag{1.1}$$

where A_f is the frontal area of one roughness element and A_s its windward wetted surface area. In the Sigal–Danberg parameter, the ratio F/F_r accounts for the roughness element density while the ratio A_f/A_s depends on the shape of the element. The power -1.6 follows from an empirical best-fitting procedure.

When considering non-regular rough walls, the difficulties in identifying geometric parameters able to fully characterize a surface are intensified. Parameters like λ and Λ_s, can be calculated in a simple way when the rough wall is made up of individual roughness elements distributed over an otherwise flat surface, while several ambiguities arise in their calculation when completely rough surfaces are considered. In such cases individual roughness elements cannot be identified and even the reference level from where to calculate the heights is not clearly defined. An extension of the Sigal–Danberg parameter Λ_s to fully irregular rough walls was proposed by van Rij, Belnap & Ligrani (2002), who replaced the ratio A_f/A_s of (1.1) with F_r/F_s, where F_r and F_s are respectively the total frontal area and the total windward wetted surface area, for all the roughness elements over a given surface F. This modified Sigal–Danberg parameter, however, loses the ability to account for the single roughness element shape, which was the principal advantage of the original parameter when compared to the solidity.

In the present paper a parameter ES is defined which accounts for the local slope of the wall roughness (a formal definition will be given in the next section), to characterize the shape of irregular rough walls. The main objective of the present analysis is to check whether a direct correlation can be established, for irregular two-dimensional rough walls, between the roughness function ΔU^+ and the new parameter accounting for the slope of the wall roughness. Leonardi *et al.* (2007) discussed the transition between k- and d-type behaviours of rough walls (Perry, Schofield & Joubert 1969), which may be related to the relative contribution of friction drag and form drag. Based on that analysis, we also investigate the relationship between these contributions and the new parameter ES.

2. The numerical experiments and discussion of the results

As in recent numerical studies of wall roughness (see e.g. Leonardi *et al.* 2003) we carry out *resolved* large-eddy simulations (LES) (also named *quasi-DNS* after Spalart *et al.* 1997) of turbulent channel flows with rough walls. These definitions hold for simulations where grid resolution is fine enough to directly resolve most of the near-wall turbulent structures.

The non-dimensional filtered Navier–Stokes equations for an incompressible flow field are:

$$\frac{\partial \overline{u}_i}{\partial t} + \frac{\partial \overline{u}_i \overline{u}_j}{\partial x_j} - \frac{1}{Re}\frac{\partial^2 \overline{u}_i}{\partial x_j \partial x_j} + \frac{\partial \overline{p}}{\partial x_i} + \frac{\partial \tau_{ij}}{\partial x_j} + \Pi\ \delta_{i1} = 0 \quad (i = 1, \ldots, 3) \tag{2.1}$$

where the overbar indicates filtered quantities, x_i is the coordinate along the ith-axis (with the streamwise direction aligned with the axis x_1), u_i is the velocity component in the ith-direction, t is time, p is the pressure, $\tau_{ij} = \overline{u_i u_j} - \overline{u}_i \overline{u}_j$ is the turbulent subgrid-scale stress (SGS) tensor, δ_{ij} is the Kronecker symbol and $Re = u^* \delta / \nu$ is the Reynolds number based on the velocity scale u^* and the channel half-height δ. The last term is the non-dimensional imposed pressure gradient driving the flow. For a rough wall, the streamwise component of the total wall stress is obtained as

$$\tau_{s,d} = \frac{1}{A}\int_A \left[-\mu \frac{\partial u_{s,d}}{\partial n}\boldsymbol{t}\cdot\boldsymbol{s} + p_d\ \boldsymbol{n}\cdot\boldsymbol{s}\right] \mathrm{d}A \tag{2.2}$$

where the index d indicates dimensional quantities, A is the wall surface, u_s is the tangential velocity component at the wall, $\boldsymbol{t}$ and $\boldsymbol{n}$ are respectively the tangential and normal vector to the wall surface element $\mathrm{d}A$, and $\boldsymbol{s}$ is the streamwise direction vector, and the velocity scale $u^* = \sqrt{\tau_{s,d}/\rho}$ is defined accounting for both the frictional and pressure contributions to the wall stress in the streamwise direction.

The integral momentum balance shows that, under statistically steady-state conditions, the force associated with the driving pressure gradient must be in balance with the overall drag, given by the streamwise component of the wall stress $\tau_{s,d}$ as $2\delta \Pi_d = 2\tau_{s,d}$, where Π_d is the dimensional imposed pressure gradient. Since in (2.1) we use δ and u^* as length and velocity scales, the non-dimensional driving pressure gradient is $\Pi = -1$.

The SGS stress tensor τ_{ij} of (2.1) is modelled using the dynamic mixed model (DMM) of Zang, Street & Koseff (1993). The governing equations are integrated using the fractional step algorithm of Zang, Street & Koseff (1994) in conjunction with a second-order-accurate finite-volume method (the details of the numerical method are reported in Lipari & Napoli 2008). The algorithm is explicit in time, and the second-order Adams–Bashforth scheme is used for the convective, diffusive and turbulent terms. The Poisson equation for the pressure is solved using a line-SOR technique in conjunction with a V-cycle multi-grid method to speed convergence. Validation tests were carried out for turbulent channel flow over smooth wall by comparing our first- and second-order statistics with the reference data of Moser, Kim & Mansour (1999). Very good agreement was found between our LES results and the DNS reference data (De Marchis 2006). In order to check the performance of the model on curvilinear grids, further tests were carried out considering a large-amplitude wavy wall, for which DNS data are available (Maas & Schumann 1996). Again, a very satisfying agreement with the reference data was achieved.

In the rough wall simulations both the upper and lower walls are corrugated in such a way as to maintain the average half-height of the channel equal to δ, and the

(*a*) First series					(*b*) Second series					(*c*) Third series				
Case	n	$\overline{r}^+$	L_w	ES	Case	n	$\overline{r}^+$	L_w	ES	Case	n	$\overline{r}^+$	L_w	ES
C_1	4	2.37	$2\pi\delta$	0.042	C_8	1	19.75	$2\pi\delta$	0.050	C_{13}	4	28.44	$1.1\pi\delta$	0.550
C_2	4	5.53	$2\pi\delta$	0.057	C_9	2	19.75	$2\pi\delta$	0.063	C_{14}	5	19.75	$\pi\delta$	0.760
C_3	4	7.90	$2\pi\delta$	0.084	C_{10}	3	19.75	$2\pi\delta$	0.149					
C_4	4	9.48	$2\pi\delta$	0.101	C_{11}	4	19.75	$2\pi\delta$	0.206					
C_5	4	13.83	$2\pi\delta$	0.145	C_{12}	5	19.75	$2\pi\delta$	0.380					
C_6	4	19.75	$2\pi\delta$	0.206										
C_7	4	28.44	$2\pi\delta$	0.300										

TABLE 1. Roughness parameters for the three sets of numerical experiments. Note that C_{11} the same as C_6.

Reynolds number $Re = u^*\delta/\nu$ is set equal to 395. Since we impose a constant driving pressure gradient, the effect of the wall roughness consists of a reduction of the flow rate and thus of the bulk velocity within the channel.

The irregular geometry of the solid boundaries is one-dimensional and generated by superposition of different sinusoidal functions with random amplitude and having maximum wavelength L_w:

$$r(x_1) = \sum_{i=1}^{n} A_n \sin\left(\frac{2n\pi x_1}{L_w}\right), \tag{2.3}$$

where $r(x_1)$ is the distance of the wall from a plane reference surface, in the $x_3 = z$ direction, n is the number of sinusoidal functions, A_n is their amplitude. The length of the domain L is set equal to $4\pi\delta$, while the channel width is set equal to π.

Three series of configurations are considered: in the first (cases C_1–C_7, table 1), the maximum wavelength L_w is kept constant, four sinusoidal functions are used and different values of the non-dimensional mean amplitude

$$\overline{r}^+ = \frac{u^*}{\nu}\frac{1}{L}\int_L |r(x_1)|\,\mathrm{d}x_1$$

of the roughness elements are considered. To illustrate a typical wall geometry of the first series, figure 1(*a*) shows case C_6 ($\overline{r}^+ = 19.75$). Note that the geometry of the upper wall and lower wall is different, due to the random generation of the amplitudes A_n.

In the second series (cases C_8–C_{12}, table 1), $\overline{r}^+ = 19.75$ and the maximum wavelength is $2\pi\delta$, whereas the number of sinusoidal functions ranges from 1 to 5. Case C_8, obtained using only one sinusoidal function ($n = 1$), is the typical *wavy wall* geometry studied in a number of papers (see for instance Armenio & Piomelli 2000 and references therein). Figure 1(*b*) shows the profiles of the bottom-surface roughness profiles for cases C_8 to C_{12}. Note that the increase in the number of sinusoidal functions results in an increase of small-scale irregularities over the wall.

In the third series (cases C_{13} and C_{14}, table 1), four sinusoidal functions are used and the maximum wavelength is changed to further increase the density of roughness corrugations compared to the first two series. In C_{13} the mean amplitude is $\overline{r}^+ = 28.44$, the wavelength is set to $1.1\pi\delta$ and the domain length is $4.4\pi\delta$ (the lower wavelength is the difference with case C_7); in C_{14} the geometric features of case C_{12} ($n = 5$ and $\overline{r}^+ = 19.75$) are maintained and the wavelength is reduced to $\pi\delta$.

The simulations were carried out using curvilinear boundary-fitted grids, of $256 \times 64 \times 64$ hexahedral cells in the streamwise, spanwise and wall-normal directions,

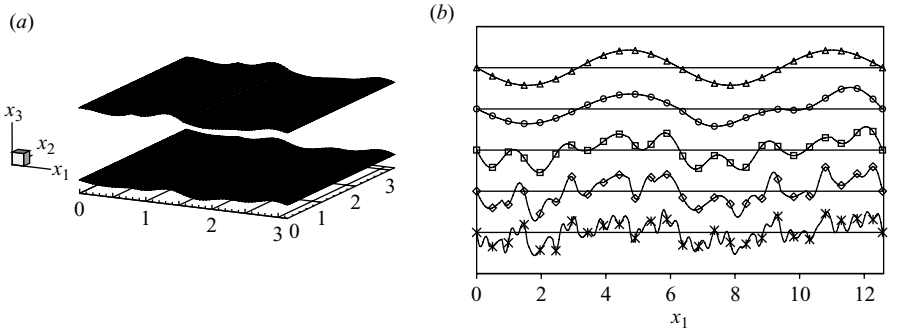

FIGURE 1. (*a*) Layout of a portion ($0 \leqslant x_1 \leqslant \pi$) of the turbulent channel domain for case C_6 (four sinusoidal functions, non-dimensional mean amplitude $\overline{r}^+ = 19.75$). (*b*) Bottom surface roughness profiles of cases C_8 to C_{12} (mean amplitude $\overline{r}^+ = 19.75$): C_8, $\triangle$; C_9, $\circ$; C_{10}, $\square$; C_{11}, $\diamond$; C_{12}, $\times$.

respectively. The cells are uniformly distributed in the streamwise and spanwise directions (with a grid spacing approximately equal to 20 wall units in both directions). In the wall-normal direction the grid cells are clustered near the walls to maintain the distance of the first grid point from the wall below one wall unit. Periodic boundary conditions are imposed in both the streamwise and spanwise directions, while no-slip conditions are imposed at the solid walls. Although the variation of the height of the wall corrugations introduces a lack of homogeneity in the streamwise direction, we can still consider the flow to be statistically homogeneous above the roughness layer on the x_1, x_2 planes and thus average the velocity fields over those planes. Since in general the vertical distribution of the grid points does not coincide with the planes of homogeneity, to calculate the statistics the instantaneous values are first interpolated at fixed distances from the channel midplane and then averaged in the planes of statistical homogeneity. Averaging is also performed in time using a window of 20 δ/u^* and taking advantage of the top/bottom symmetry. To preserve accuracy, third-order splines are used for spatial interpolation of the velocity fields. The statistics are calculated for the fluid region within the extreme peaks of the bottom and top walls.

The wide range of irregular walls considered herein gave different values of the roughness functions, while maintaining the logarithmic profile in the flow interior. The non-dimensional profiles of the streamwise mean velocity are shown in semi-logarithmic plots in figure 2(*a*) for the first set of simulations and in figure 2(*b*) for the other sets. The non-dimensional wall-normal coordinate z^+ is measured from the horizontal flat plane on which the sinusoidal functions are superimposed and the velocity profiles start from different values of the non-dimensional wall-normal coordinate, corresponding to the wall-normal location of the maximum peak of the wall corrugation. In figure 2(*a*, *b*) we also plot the equivalent plane-channel flow velocity profile at $Re_\tau = 395$ and the straight line dividing the transitional and the fully rough regimes. In figure 2(*a*) both transitionally and fully rough behaviours are present: cases C_1 to C_5, being above the line, are in the transitional regime, while cases C_6 and C_7 are in the fully rough regime. For a given number of wave modes, the downward shift of the log-law region increases with $\overline{r}^+$, which is a well-known effect of roughness. Figure 2(*b*) shows that, when the level of roughness is varied by increasing the number of wavy modes, a substantial increase of the roughness function ΔU^+ is obtained although $\overline{r}^+$ remains constant. Also in this case, both transitionally rough (cases C_8 and C_9) and fully rough (cases C_{10}

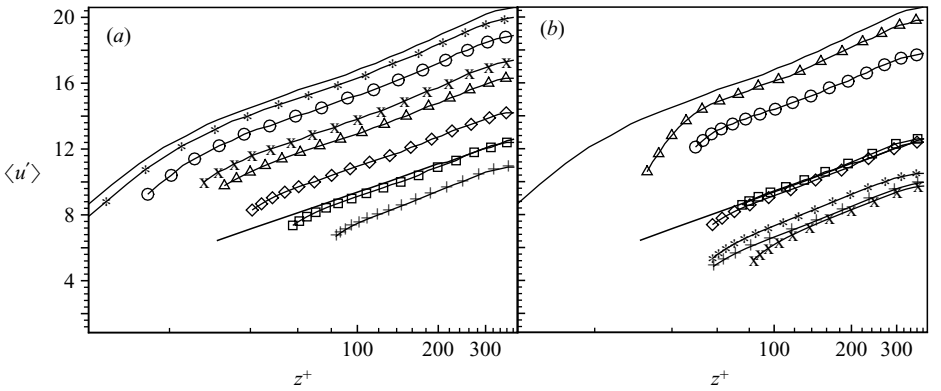

FIGURE 2. Wall-normal profiles of the non-dimensional mean streamwise velocity u^+ for the three sets of simulations. (*a*) First series: Smooth wall: thin solid line. Limit of the fully rough wall ($\langle u^+ \rangle = (1/\kappa)\log z^+/k_s^+ + 8.5$ with $k_s^+ = 70$): bold solid line. C_1: *. C_2: ○. C_3: ×. C_4: △. C_5: ◇. C_6: □. C_7: +. (*b*) Second and third series: Smooth wall: thin solid line. Limit of the fully rough wall: bold solid line. C_8: △. C_9: ○. C_{10}: □. C_{11}: ◇. C_{12}: *. C_{13}: ×. C_{14}: +.

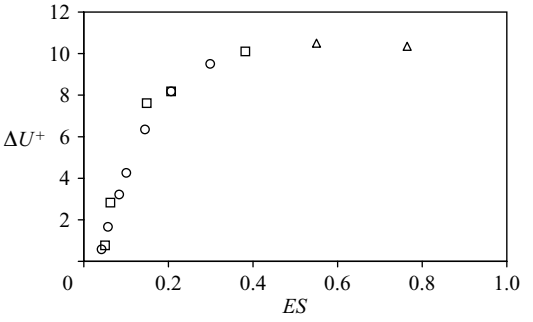

FIGURE 3. Dependence of the roughness function ΔU^+ on the effective slope of the wall corrugations, ○, cases $C_1 - C_7$; □, cases $C_8 - C_{12}$; △, cases $C_{13} - C_{14}$.

to C_{14}) behaviours are present. Here the roughness function ΔU^+ is not directly related to the mean amplitude $\overline{r}^+$, but rather to the variation of the density of roughness corrugations. The results of the third series of simulations (figure 2*b*) show that, beyond a certain level of density of wall corrugations, the roughness function starts to decrease, a well-known effect of sheltering of one element by the other.

To account for both the height and density of the roughness corrugations, a parameter, called the *effective slope*, is introduced:

$$ES = \frac{1}{L}\int_L \left|\frac{\partial r}{\partial x_1}\right| \mathrm{d}x_1. \tag{2.4}$$

It can be shown that ES is twice the solidity, and is easier to use in the general cases of randomly distributed wall roughness.

In figure 3 the roughness function ΔU^+ is plotted against the effective slope ES for all cases considered herein. Here the roughness functions were obtained by calculating the mean offsets of the velocity profiles, in the range $z^+ = 100 - 200$, from the smooth wall profile. In the first series of simulations (C_1 to C_7) the effective slope grows from 0.05 to 0.3 with the amplitude of wall corrugations (see table 1), while in

the second series (C_8 to C_{12}) it increases with the number of sinusoidal functions, from 0.042 to 0.38. In the third series the largest values of ES are attained, 0.55 in case C_{13} and 0.76 in case C_{14}. A clear dependence of the roughness function ΔU^+ on the effective slope of the wall corrugations can be easily identified, irrespective of the specific geometry (number of sinusoidal functions, mean amplitude of the wall corrugations and maximum wavelength of the sinusoidal functions) of the cases investigated. Specifically ΔU^+ increases linearly up to about $ES \sim 0.15$, follows a nonlinear curve for larger values of ES up to a maximum for $ES \sim 0.55$ and then weakly decreases. This behaviour is in agreement with the literature results for regular roughness geometry (as reported in Jimenez 2004), which showed the decrease of the roughness function beyond a certain value of solidity.

Note that the decrease of ΔU^+ beyond the maximum value obtained in our simulations is much smoother than in the literature; this behaviour is probably because we study irregular roughness geometry, making the mutual sheltering effect of the single corrugations less pronounced. Moreover, previous studies considering wall roughness with regular distributions of identical elements identified the maximum of the roughness function for solidity $\lambda \sim 0.15$ (see figure 1*a* in Jimenez 2004) which corresponds to $ES \sim 0.3$. As can be seen in figure 3, we found the maximum in ΔU^+ for values of ES near 0.55, corresponding to $\lambda \sim 0.275$, well beyond the peak value obtained for regularly roughened walls with two-dimensional spanwise obstacles. This is probably because, when the roughness is randomly distributed, with an ensemble of peaks of different heights and with a range of densities along the streamwise direction, a selective behaviour may take place, which makes the projected areas of very dense and small elements less important than those of the largest elements. In this case, although the small elements contribute to the value of ES, they do not alter the main characteristics of the flow and a further increase of ΔU^+ is observed for a wider range of values of ES. Clearly this effect cannot occur for rough walls made of regularly distributed identical elements. Finally, note that the slope of the curve in figure 3 strongly decreases for $ES \geqslant 0.15$, which in the cases investigated herein corresponds to the start of the fully rough regime (C_6, C_7 and C_{10} to C_{14}).

It is not straightforward to make a direct quantitative comparison with literature data, since we analyse random corrugations that cannot be reduced to a series of well-defined elements, whereas literature studies are mainly concerned with regular roughness made up of identical elements; this makes it difficult to unequivocally find a roughness length scale comparable with that of regular roughness, namely the height of the elements. Leonardi, Orlandi & Antonia (2007) considered walls roughened with two-dimensional square bars placed at regular streamwise intervals; for given values of the pitch to height ratio w/k, corresponding to $ES = 2k/(w + k)$, they found a dependence of the roughness function on the Reynolds number and thus on the height k^+ of the roughness elements in wall units, which is a geometric parameter without a direct counterpart in our geometries. If we use $2\overline{r}^+$ as length scale (the mean trough-to-crest distance) and compare our results with the data of Leonardi *et al.* (2007) we find a value of the roughness function of about 30% less than theirs. On the other hand, analogous comparison with the experimental measurements of Krogstad & Antonia (1999), who used circular rods to regularly roughen the wall, results in an underprediction of the roughness function obtained with $ES = 0.55$ of about 5%. These differences, besides being due to the irregularity of roughness in this paper, depend on the fact that these authors found a clear dependence of the roughness function on the height k^+ of the roughness elements in wall units), which has no direct counterpart in our geometries. The mean amplitude $\overline{r}^+$ is conceptually different

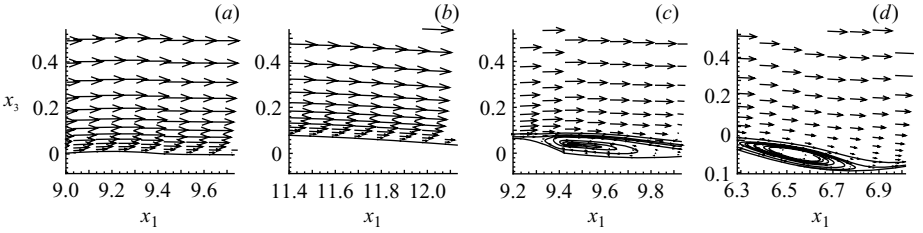

FIGURE 4. Detail of the velocity fields averaged in time and in the spanwise direction downwind of roughness peaks for cases C_1 (*a*), C_8 (*b*), C_5 (*c*) and C_{10} (*d*). Some streamlines are plotted for C_5 and C_{10} to highlight the occurrence of separation downwind of the roughness peaks.

from k^+, which depends only on the peaks of the roughness elements, whereas $\overline{r}^+$ contains a wide range of local corrugation heights.

In our simulations the range of variation of the mean amplitude $\overline{r}^+$ is small and this explains the relatively weak dependence of ΔU^+ on $\overline{r}^+$. Nevertheless, this dependence is within the range predicted in the literature. Consider for instance, case C_{10}, having a mean amplitude 1.42 times larger than C_5 and an almost identical value of ES. Assuming the ratio between the equivalent sand roughnesses k_s to be equal to the ratio between the mean amplitudes, the difference in the roughness function can be estimated as $\Delta U_{10}^+ - \Delta U_5^+ = (1/\kappa)\ \log(k_{s10}^+/k_{s5}^+) = (1/\kappa)\ \log\ 1.42 \approx 0.9$ where κ is the von Kármán constant (for a discussion see Jimenez 2004). This value is very close to the difference obtained in the simulations, which is roughly equal to one unit.

Finally, the analysis of figure 3 shows that cases C_1 and C_8 have approximately the same ES, being characterized by strong geometric differences (C_8 is a small-amplitude wavy wall, C_1 is a 4-mode wave with mean amplitude one order of magnitude smaller than C_8), and exhibit equivalent behaviour with respect to the roughness function. This can be attributed to the effective slope of the wall producing in both cases non-separated flows near the wall, thus having equivalent effects on the flow field, as shown in figure 4(*a*, *b*) where a sketch of the time- and spanwise-averaged velocity fields downwind of roughness peaks are plotted for cases C_1 and C_8. On the other hand, case C_5 (four wave modes and $\overline{r}^+ = 13.83$) and case C_{10} (three wave modes and $\overline{r}^+ = 19.50$) have similar ES and behave similarly with respect to the roughness function. This analogous behaviour can be explained by the fact that in both cases localized flow separation occurs behind the crests, as depicted in figure 4(*c*, *d*). These results clearly indicate that the effective slope ES is one of the parameters well suited to characterize the geometry of non-regular wall roughness for the evaluation of the roughness function ΔU^+. Specifically, our results corroborate and extend the literature findings on the role of parameters such as the solidity λ and the Sigal–Danberg parameter.

To give a physical explanation of the dependence of the roughness function ΔU^+ on the parameter ES, we discuss the results of our simulations in the light of the recent findings of Leonardi *et al.* (2007) on the relative importance of the friction and pressure contributions to the total drag in regular rough geometry. In figure 5 the friction-drag coefficient $C_f = D_f/\rho u^{*2}$ and the pressure-drag coefficient $C_p = D_p/\rho u^{*2}$ are plotted against ES for cases C_1 to C_{14}. D_f and D_p are the streamwise components of the friction and pressure stress, respectively. Note that since our simulations were carried out with constant imposed pressure gradient, the momentum balance in the streamwise direction gives $C_f + C_p = |\Pi| = 1$. A clear dependence of the friction- and pressure-drag coefficients on the parameter ES is easily identified. The increase of the effective slope in cases C_1 to C_7 results in a progressive

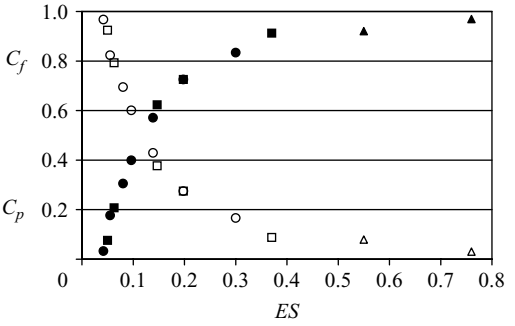

FIGURE 5. Dependence of the pressure drag C_p (filled symbols) and of the friction drag C_f (open symbols) on the effective slope of the wall corrogations. ○, cases C_1 to C_7; □, C_8 to C_{12}; Δ, C_{13} and C_{14}.

reduction of the friction contribution to the drag and in the corresponding growth of the pressure drag. This is due again to the occurrence of more local separation effects downstream of the local wall peaks as the slope of roughness corrugations increases. Analogously, in cases C_8 to C_{12}, the effective slope grows with the increase of the number of wave-modes, since the mean height remains unchanged from case to case. Correspondingly, the relative contribution of the pressure drag increases due, again, to the increase of local downward separation behind the local peaks. Note that the data collapse onto single curves for the three series of simulations, thus demonstrating that the effective slope of the wall corrugations is an appropriate geometric parameters to describe the behaviour of rough walls, independently of the mean height and distribution of the roughness elements.

Analysis of figure 5 indicates that, for the geometric configurations analysed herein, a value of the effective slope of about $ES = 0.12$ identifies the condition of equality of the friction- and pressure-drag contributions, while for higher values the pressure drag dominates over the friction contribution to the total drag. Note that this value is very close to the value $ES \sim 0.15$ beyond which a fully-rough behaviour was observed in figure 2(a, b) , together with a change in the slope of the curve $\Delta U^+ = f(ES)$. Although our results indicate that the value of $ES \sim 0.12-0.15$ at which friction- and pressure-drag contributions are in balance determines the change of the slope of the curve $\Delta U^+ = f(ES)$ and the change of regime from transitional to rough, further studies are required to identify a general threshold value of the effective slope for different values of the Reynolds number and for general three-dimensional corrugations.

3. Conclusions

In this paper we have investigated the behaviour of the roughness function ΔU^+ in a turbulent channel flow with irregular rough walls obtained by superposition of sinusoidal functions of different amplitude and wavelength. Numerical quasi-DNS simulations showed that ES is one of the geometric parameters able to represent the effect of a rough wall on the roughness function. Our study demonstrates that rough walls constructed in very different ways, characterized by different mean heights and spatial distribution of the roughness corrugations, exhibit very similar behaviour if they have similar values of the effective slope. The results of the present study agree with previous studies of regular distributions of roughness elements on the role of geometrical parameters such as the solidity, while extending them to the general case of irregular rough walls. The peak value of the roughness function ΔU^+ appears shifted toward values of the effective slope larger than the equivalent value available in literature

for regular rough walls. This is attributed to the effect of irregularity, that produces a selective behaviour of the roughness corrugations with respect to the increase of drag.

It was found that the effective slope determines the relative importance of friction drag and pressure drag. The increase of ES and thus of the corrugation density gives a reduction of the friction drag and a corresponding growth of the pressure drag, irrespective of other geometric features of the rough wall. Specifically, our study shows a value $ES \sim 0.12$–0.15 such that pressure drag and friction drag contribute equally to the total drag. In our study, this value has been found to determine the change of regime from transitionally to fully rough and the change of the slope of the curve $\Delta U^+ = f(ES)$, from linear behaviour ($ES \leqslant 0.15$) to smooth nonlinear behaviour $ES \geqslant 0.15$. Additional studies are required to extend our findings, considering different values of the Reynolds number and three-dimensional irregular roughness.

REFERENCES

Armenio, V. & Piomelli, U. 2000 A lagrangian mixed subgrid-scale model in generalized coordinates. *Flow Turbul. Combust.* **65**, 51–81.

Colebrook, C. F. & White, C. M. 1937 Experiments with fluid friction in roughened pipes. *Proc. R. Soc. Lond.* **161**, 367–381.

De Marchis, M. 2006 Numerical study on the effects of wall roughness on the turbulent flow fileds (in italian). PhD thesis, University of Palermo, Palermo.

Jimenez, J. 2004 Turbulent flows over rough walls. *Annu. Rev. Fluid Mech.* **36**, 173–196.

Krogstad, P. A. & Antonia, R. A. 1999 Surface roughness effects in turbulent boundary layers. *Exp. Fluids* **27**, 450–460.

Leonardi, S., Orlandi, P. & Antonia, R. A. 2007 Properties of d-type and k-type roughness in a turbulent channel flow. *Phys. Fluids* **19**, 125101.

Leonardi, S., Orlandi, P., Smalley, P., Djenidi, L. & Antonia, R. A. 2003 Direct numerical simulations of turbulent channel flow with transverse square bars on one wall. *J. Fluid Mech.* **491**, 229–238.

Lipari, G. & Napoli, E. 2008 The impacts of the ale and hydrostatic-pressure approaches on the energy budget of unsteady free-surface flows. *Comput. Fluids* **37**, 656–673.

Maas, C. & Schumann, U. 1996 Direct numerical simulation of separated turbulent flow over a wavy boundary. In *Flow Simulation with High Performance Computers, II.* (ed. E. H. Hirschel) Notes on Numerical Fluid Dynamics, vol. 52, pp. 227–241, see ER-COFTAC database, Case 77, http://cfd.mace.manchester.ac.uk/ercoftac/index.html

Moser, R. D., Kim, J. & Mansour, N. M. 1999 Direct numerical simulation of turbulent channel flow up to $Re = 590$. *Phys. Fluids* **11**, 943–945.

Perry, A. E., Schofield, W. H. & Joubert, P. N. 1969 Rough wall turbulent boundary layers. *J. Fluid Mech.* **37**, 383–413.

van Rij, J. A., Belnap, B. J. & Ligrani, P. M. 2002 Analysis and experiments on three-dimensional, irregular surface roughness. *J. Fluids Engng* **124**, 671–677.

Schlichting, H. 1936 Experimentelle untersuchungenz rauhigkitsproblem. *Ing. Arch.* **7**, 1–34.

Shockling, M. A., Allen, J. J. & Smits, A. J. 2006 Roughness effects in turbulent pipe flow. *J. Fluid Mech.* **564**, 267–285.

Sigal, A. & Danberg, J. E. 1990 New correlation of roughness density effect on the turbulent boundary layer. *AIAA J.* **28**, 554–556.

Spalart, P. R., Jou, W.-H., Strelets, M. & Allmaras, S. R. 1997 Comments on the feasibility of les for wings, and on a hybrid rans/les approach. *First AFOSR Intl. Conference on DNS/LES, Advances in DNS/LES*, pp. 137–147.

Zang, Y., Street, R. L. & Koseff, J. R. 1993 A dynamic mixed subgride-scale model and its application to turbulent recirculating flows. *Phys. Fluids* **12**, 3186–3196.

Zang, Y., Street, R. L. & Koseff, J. R. 1994 A non-staggered grid, fractional step method for time-dependent incompressible navier-stokes equations in curvilinear coordinates. *J. Comput. Phys.* **114**, 18–33.